

# Atomic Structure and Formation Mechanism of Sub-Nanometer Pores in 2D Monolayer MoS<sub>2</sub>

*Shanshan Wang<sup>1</sup>, Huashan Li<sup>2</sup>, Hidetaka Sawada<sup>1,3,4</sup>, Christopher S. Allen,<sup>1,4</sup> Angus I. Kirkland<sup>1,4</sup>,  
Jeffrey C. Grossman<sup>2\*</sup>, Jamie H. Warner<sup>1\*</sup>*

<sup>1</sup>Department of Materials, University of Oxford, Parks Road, Oxford, OX1 3PH, United Kingdom

<sup>2</sup>Department of Materials Science and Engineering, Massachusetts Institute of Technology, 77  
Massachusetts Avenue, Cambridge, MA, 02139, USA.

<sup>3</sup>JEOL Ltd., 3-1-2 Musashino, Akishima, Tokyo 196-8558, Japan

<sup>4</sup>Electron Physical Sciences Imaging Center, Diamond Light Source Ltd, Didcot, Oxfordshire, OX11  
0DE, United Kingdom

Email: [\\*Jamie.warner@materials.ox.ac.uk](mailto:*Jamie.warner@materials.ox.ac.uk); [jcg@mit.edu](mailto:jcg@mit.edu)

## **Abstract**

We use electron-beam nanofabrication to create sub-nanometer (sub-nm) pores in 2D monolayer MoS<sub>2</sub> with fine control over the pore size down to 0.6nm, corresponding to the loss of a single Mo atom and surrounding S atoms. The sub-nm pores are created *in-situ* with 1nm spatial precision in the MoS<sub>2</sub> lattice by control of the Angstrom sized probe in an aberration corrected scanning transmission electron microscope with real time tracking of the pore creation. Dynamics of the sub-nm pore creation are captured at the atomic scale and reveal the mechanism of nanopore formation at accelerating voltages of 60 and 80kV to be due to displacing a Mo atom from the lattice site onto the surface of the MoS<sub>2</sub>. This process is enabled by the destabilization of the Mo bonding from localized electron beam induced S atom loss. DFT calculations confirm the energetic advantage of having the ejected Mo atom attach on the sheet surface rather than being expelled into vacuum, and indicate sensitivity of the

nanopore potential as a function of the absorption position of the ejected Mo atom. These results provide detailed atomic level insights into the initial process of single Mo loss that underpins the nucleation of a nanopore and explains the formation mechanism of sub-nm pores in MoS<sub>2</sub>.

**KEYWORDS** nanopores, MoS<sub>2</sub>, 2D, STEM, defects

A wide variety of 2D materials are now the subject of active research, with different chemical composition, structure and properties.<sup>1–3</sup> Graphene is composed of sp<sup>2</sup> bonded carbon with single atom thickness, while hBN has similar structure but with N and B atoms replacing the carbon atoms within the hexagonal lattice. Recent studies of monolayer transition metal dichalcogenides (TMDs), such as MoS<sub>2</sub>, have received significant interest due to their direct band gap that provides semiconducting behaviour and light emission in the visible spectrum.<sup>4–6</sup> Consequently, there has been intensive research into the use of 2D MoS<sub>2</sub> in electronics and opto-electronics.<sup>7–10</sup> Importantly, defects and dopants in monolayer TMDs influence their properties and the ability to spatially control defect formation is integral to successful nanoengineering of these.<sup>11–19</sup>

The ultrathin nature of 2D materials makes them appealing as membranes for a wide range of applications, such as water desalination,<sup>20–22</sup> alcohol concentration,<sup>23</sup> gas filtration,<sup>24</sup> DNA sequencing,<sup>25,26</sup> and biomolecular translocation.<sup>27</sup> Nanopores in graphene have been used to restrict/allow atomic and molecular transport through the 2D material to provide separation. In water desalination, only the small H<sub>2</sub>O molecules are able to pass through suitable sized nanopores in graphene, leaving behind the impurities. Similar filtration can be obtained for mixed gaseous species, where a specific small gas molecule can pass a suitable sized pore. Membranes containing nanopores are also used in liquid environments to provide holes for specific molecules to enter and propagate through the membrane.<sup>28,29</sup> By monitoring the ionic current flowing through the pore, it is possible to detect current changes associated with DNA translocation.<sup>30</sup> Recent work has shown that monolayer MoS<sub>2</sub> offers better stability than graphene for translocation studies of DNA through nanopores due to

reduced hydrophobic interactions between the DNA and the membrane surface.<sup>31</sup> Currently, nanopores in 2D materials are generally produced either by chemical etching (electrochemical reaction,<sup>29</sup> selective oxidation,<sup>32,33</sup> reactive-ion/molecule etching,<sup>34,35</sup>) or by focused high energy particle bombardment (electron beam irradiation,<sup>36–44</sup> focused ion beam drilling,<sup>45</sup> etc.). Although chemical approaches may have advantage of cost-efficiency, short duration of processing, and scalability, they are unable to accurately control the location of a nanopore with nanoscale precision and do not allow real-time monitoring of the nanopore size and configuration at the atomic level.

Focused electron beam irradiation in transmission electron microscopy (TEM) has been used to pattern electrode materials and cut graphene and nanotubes into different shapes. Creating nanopores in 2D materials with electron beams is often done using TEM, because it provides excellent precision and direct real time *in-situ* atomic level monitoring. The high energy electrons transfer energy to the 2D material to remove atoms and produce a hole.<sup>46</sup> Increasing the beam current density and the energy of electrons can typically control the hole drilling within a short timeframe. Drilling holes in graphene is more challenging than in MoS<sub>2</sub> due to the propensity of surface adsorbed carbon atoms to fill in the vacancy structures formed and also complicate the atomic removal process due to chemical etching effects.<sup>38</sup> Most work on nanopore introduction into 2D materials has used TEM in a phase contrast imaging mode, with a relatively large beam diameter of typically 10-20nm.<sup>47</sup> This is suitable only for the fabrication of a single nanopore and cannot be used to create nanopore arrays in close proximity approaching sub-10nm. Prior work on producing nanopore arrays in graphene contained a large amount of surface hydrocarbon contamination that is known to rapidly react under the electron beam and this will assist the nanopore production.<sup>43</sup> Aberration corrected Scanning Transmission Electron Microscopy (AC-STEM) provides a focussed electron beam of atomic size that can interact sequentially with single atoms in a material. Prior work using a STEM probe has shown that thin graphene ribbon structures can be cut from graphene and that small holes can be drilled into carbon nanotubes.<sup>37,42</sup> Nanoconstrictions in black phosphorous have also been fabricated using a

STEM probe.<sup>44</sup> Recent research by Lin *et al.* used STEM to fabrication multiple nanopores in MoS<sub>2</sub> with close proximity, but were not able to demonstrate repeatable controlled fabrication of sub-nm pores, nor study the atomic scale dynamics of the initial formation mechanisms.<sup>48</sup> While the methods of electrochemical etching and oxidization may create some small sub-nm scale pores in 2D materials, they lack the ability to see the process in real time to understand the formation mechanism atomic scale, allowing only postulations regarding the possible formation mechanisms of atom loss.<sup>29,32</sup> More understanding is needed on the atomic level insights to the formation of sub-nm pores and their structure and dynamics.

Because MoS<sub>2</sub> consists of both heavy Mo and light S atoms, the removal of atoms from the lattice by the electron beam is primarily associated with loss of S atoms as demonstrated by recent calculations and experiments for 80kV electrons.<sup>49</sup> An accelerating voltage of 60kV also leads to S vacancies in MoS<sub>2</sub> and the subsequent loss of Mo atoms from the material with increasing beam dose.<sup>50,51</sup> This introduction of S vacancies in the material can alter its structural form and properties.<sup>14,52</sup> In the work presented here, we examine how ultra-small sub-nm nanopores can be controllably introduced into monolayer MoS<sub>2</sub> using the electron probe in an AC-STEM. While the use of a focussed electron beam to create nanopores in 2D materials is not new, its use to create sub-nm pores in MoS<sub>2</sub> has yet to be achieved. The ability to place sub-nm pores in close proximity to each other has yet to be demonstrated. We study the detailed atomic structure and real time dynamics of these sub-nm nanopores in MoS<sub>2</sub> to understand the formation mechanism that underpins the initial nucleation process.

## Results and Discussion

We were able to introduce both single sub-nm pores as well as multiple sub-nm pores set out into a patterned array in MoS<sub>2</sub> with separation distances less than 5nm. The monolayer MoS<sub>2</sub> was grown by chemical vapour deposition using previously reported methods and transferred onto a SiN

TEM grid with arrays of  $2\mu\text{m}$  holes.<sup>53</sup> The  $\text{MoS}_2$  was cleaned by heating in activated carbon to remove adsorbed hydrocarbons. This was essential because the presence of surface adsorbed hydrocarbons reduced the sputtering of S atoms to create the nanopores. Dirty  $\text{MoS}_2$  was ineffective for nanopore formation, likely associated with the changes in the sputtering thresholds associated with adding a hydrocarbon layer onto the  $\text{MoS}_2$ , as was recently reported using graphene to protect  $\text{MoS}_2$  from electron beam damage.<sup>51</sup>

Figure 1 shows a schematic illustration of the nanopore fabrication process. Clean areas were first identified at low magnification and then an image is taken of the areas at higher magnifications using a fast scan rate in order to minimize beam induced damage before any nanopore drilling begins. A scan region of  $\sim 1\text{nm} \times 1\text{nm}$  is selected in a specific region and then the beam slowly scanned across the region to form the nanopore. The size of the nanopore can then be further increased by another controlled electron beam exposure. To extend this beyond simple single nanopore production, we translated the boxed area that defined the drilling region to a new position and this enabled us to sequentially drill multiple nanopores one-by-one in arbitrary patterns, including 2D arrays. Further details are found in the methods section.

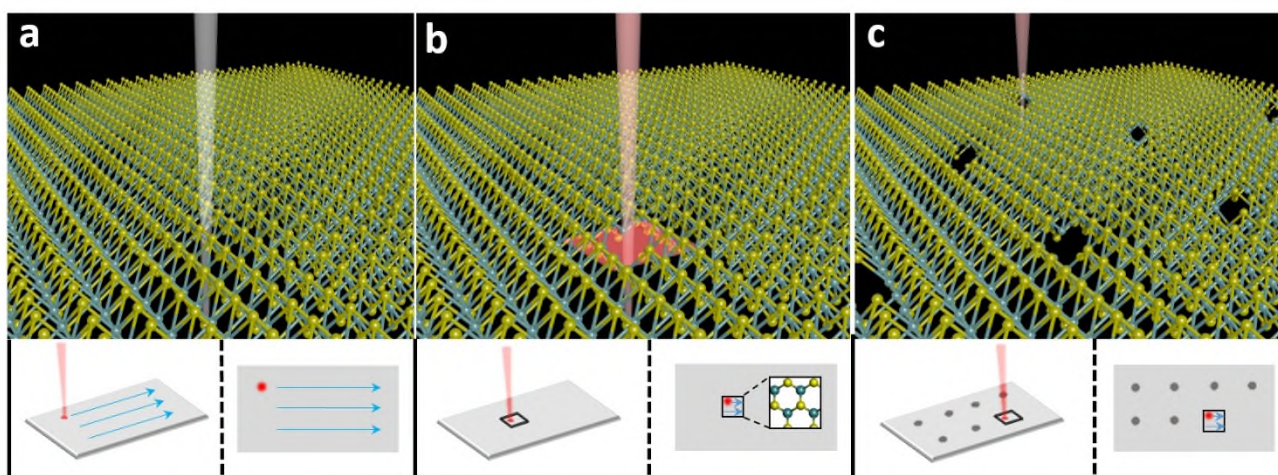


**Figure 1.** Schematic illustration of the electron beam drilling process to create sub nanometer holes in monolayer  $\text{MoS}_2$  and the extension into patterned arrays. (a) A fast-scan ADF-STEM image is taken to

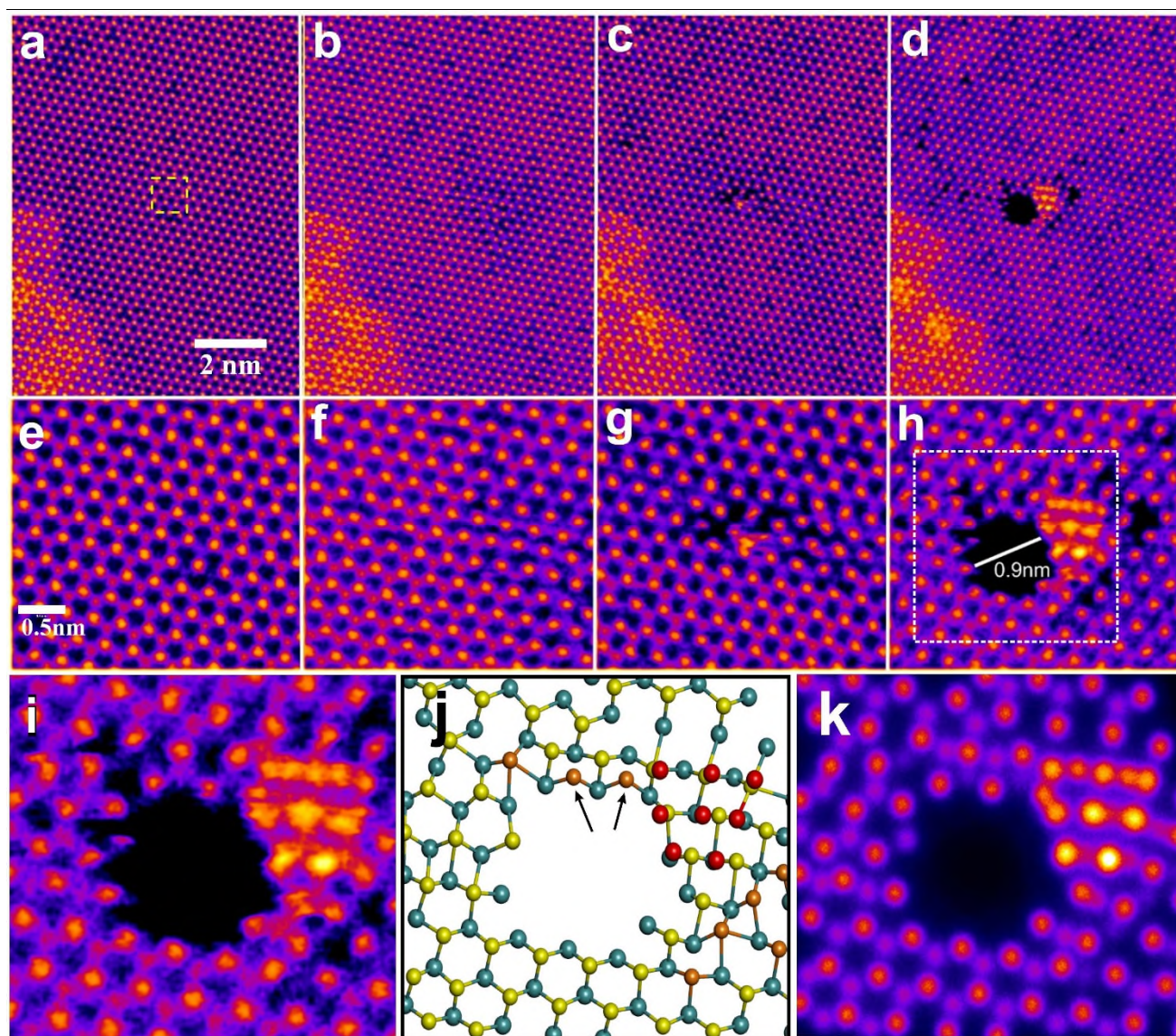
establish the broader area for drilling. (b) A small boxed region is defined and scanned at a slow rate to induce S loss. (c) The boxed region is moved to a new location to drill another hole in the material. Once all holes are drilled, the entire area is imaged by ADF-STEM to reveal the structures produced.

Figure 2 shows the step-by-step creation of a sub-nanometer pore within a clean MoS<sub>2</sub> area using an 80kV accelerating voltage. The ADF-STEM image in figure 2a shows some amorphous hydrocarbon surface residue in the bottom left corner, which was used to align the images frame by frame for reference. After the first 10s of drilling (figure 2b) the region shows an agglomeration of S vacancies within the exposed location. After the second 10s drilling (figure 2c) the degree of damage in the area has increased and the high magnification image (figure 2g) shows that a single Mo atom has been displaced from the lattice to the surface, evident as the bright contrast spot. This is the initial trigger that escalates further to produce the nucleation of the nanopore. Without the ejection of the Mo atom onto the surface of the MoS<sub>2</sub>, a nanopore will not be created. By irradiating only a small area we are concentrating the S vacancy production into this area and this leads to the destabilization of the Mo bonding to the surrounding atoms and eventually a single Mo atom is ejected to the surface within this 1nm region.

A further 10s of drilling (figure 2d) leads to the formation of a small nanopore that has a width of ~0.9nm. Bright spots are evident in figure 2d and are associated with multiple Mo atoms that have been ejected to the surface of MoS<sub>2</sub>. The number of surface bound Mo atoms also correlates with the total number that are lost from the nanopore hole, indicating that Mo atoms are not directly ejected into the vacuum to create the hole. Examination of the ADF-STEM image in figure 2h shows that the edge of the nanopore is terminated by Mo atoms, with the S atoms having been sputtered out by the electron beam. Therefore the edge chemistry of the nanopores formed by electron beam drilling is Mo rich. The magnified view of the nanopore, figure 2i, reveals that there is Mo termination along six zigzag lattice directions, indicating that reconstruction has occurred for the S-terminated zigzag edges. The atomic model in figure 2j, was constructed based on the ADF-STEM image in figure 2i, and the



image simulation is shown in figure 2k. The good match between the simulation and experimental image indicate that approximately 8 Mo atoms have been ejected to the surface, which is about the same number as those missing in the pore. The black arrows in figure 2k show the region where reconstruction has occurred to maintain Mo termination along the zigzag direction that is meant to have S-termination.



**Figure 2.** ADF-STEM images showing step-by-step drilling of a nanopore in monolayer MoS<sub>2</sub> using 80kV accelerating voltage. (a) Clean MoS<sub>2</sub> region before drilling. The yellow dashed box shows the area that is subjected to subsequent drilling. (b) ADF-STEM image taken after 10s of drilling in the yellow boxed region. (c) ADF-STEM image after a further 10 s of drilling in the same area. (d) ADF-STEM image taken after another

10 s of drilling in the same area. (e)-(h) Magnified ADF-STEM images of the central regions that were drilled in (a)-(d). (i) Magnified view of the nanopore shown in (h), indicated by the white dashed box. (j) Atomic model constructed based on the ADF-STEM image in (i). (k) Image simulation based on the atomic model in (j).

The size of the nanopores can be controlled by the total electron beam dose within the defined drilling region, achieved by using slower scan rates in the defined region that led to Mo displacement in a shorter time. In figure 3, the scanning rate is halved compared to that used in figure 2, leading to a 10s drilling time to produce nanopores. Figure 3a shows an ADF-STEM image of the area before drilling and the yellow box indicates the scan area for drilling. Figure 3b shows the ADF-STEM image of this area after 10s drilling, with a higher magnification image shown in figure 3f. Loss of S atoms was observed within the drilled region, but no hole had yet formed. Another 10s of drilling in the same area was performed and the ADF-STEM image taken after this process shows the formation of an ultra-small nanopore (figure 3c) with a higher magnification image shown in figure 3g. Figure 3d and 3e show ADF-STEM images taken immediately after that in figure 3c, demonstrating that the nanopore does not further increase in size and is stable under the imaging conditions used at 80kV. Figure 3g shows that a Mo atom is displaced to the surface adjacent to the hole. The diameter of the hole is  $\sim 0.6\text{nm}$ , measured as the center-to-center of the contrast associated with the Mo atoms that define the edge. Figures 3h and 3i show the DFT relaxed atomic model of the nanopore and its corresponding ADF-STEM image simulation is a good match to the experimental ADF-STEM image in the cyan rectangular box in figure 3g. The DFT calculation indicates the energetic advantage of having the ejected Mo atom relocate onto the  $\text{MoS}_2$  surface and bind with surrounding Mo and S atoms. Figures 3j-m reveals how the single Mo atom is displaced from the lattice position by the electron beam to form an ultra-small nanopore, as well as the migration path of this Mo atom on the  $\text{MoS}_2$  surface (also see figure S1). This sequence shows that the S atoms neighbouring this Mo atom were first removed by the e-beam (figure 3j), which decreased the stability of the single Mo atom in the lattice. Subsequently, the Mo escaped from its original atomic position. Rather than being ejected into the



vacuum, it relocated onto the nearby MoS<sub>2</sub> surface and subsequently migrated, preferably residing on positions between two Mo atomic sites on the MoS<sub>2</sub> surface (figures 3l, m).

A high signal-to-noise ADF-STEM image of a sub-nanometer pore is shown in figure 3n. The central Mo atom along with its three nearest neighbour S pairs are missing, leaving three Mo-terminated zigzag edges. The DFT-relaxed atomic model (figure 3o) with the corresponding ADF image simulation (figure 3p) show good agreement with the experimental observation. Line profiles along three zigzag orientations around the nanopore, figure 3q, are used to determine the Mo-Mo interatomic distances, figure 3r, and show that the distances between two unsaturated Mo atoms on the nanopore edge along three zigzag directions are all larger than the pristine Mo-Mo distance ( $\sim 3.1\text{\AA}$ ), similar to pentagonal reconstructions in graphene nanopores.<sup>36</sup>

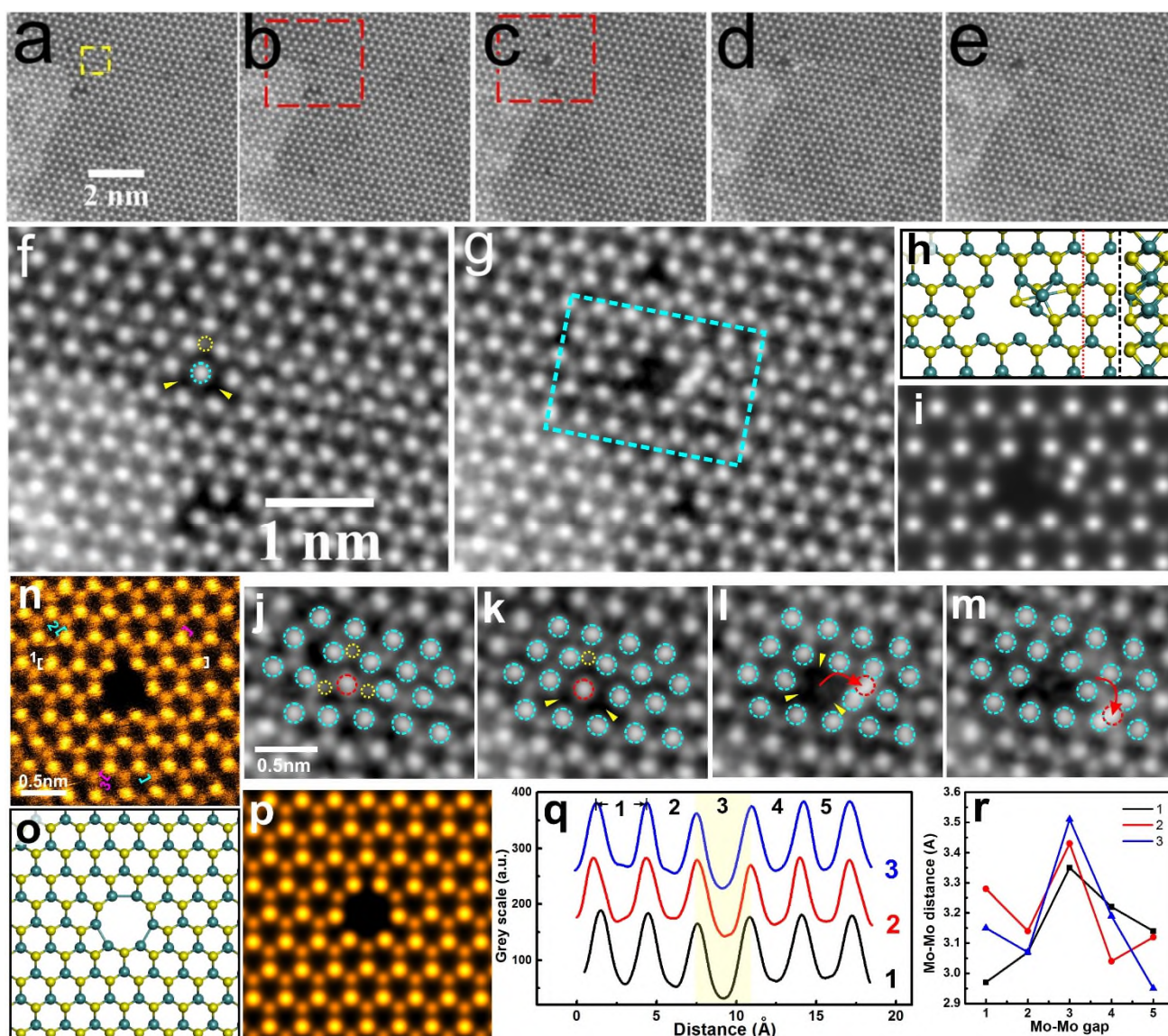


**Figure 3. Ultra-small nanopore formation by displacing a single Mo atom. Scan speed is faster compared**

**to figure 2, which reduces beam current density. Drilling time was kept at 10s. 80kV accelerating voltage**

(a)-(e) Step by step process of creating a single sub-nanometer pore in MoS<sub>2</sub> (a) ADF-STEM image showing

the area of MoS<sub>2</sub> before drilling. (b) ADF-STEM image taken after 10s drilling. (c) ADF-STEM image taken

after a further 10s drilling. A small nanopore has been formed by the displacement of a single Mo atom. (d) and

(e) Images taken after (c) to show the stability of the nanopore. (f) Higher magnification ADF-STEM image of

the region indicated by the red dashed box in (b) showing the increased loss of S atoms within the region drilled.

The two yellow arrows indicate the removal of two pairs of S atoms which were originally coordinated to the

central Mo atom marked by the dashed cyan circle, while the yellow dashed circle shows the residual S atom

bound to the central Mo atom. (g) Higher magnification image of the region indicated by the red dashed box in

(c) showing the formation of an ultra-small nanopore by the displacement of a Mo atom to the surface (bright contrast spot located on the right of the hole). (h) DFT-calculated atomic model showing one of the energetically favoured structures for the ejected Mo atom on the surface of MoS<sub>2</sub>. (i) ADF-STEM image simulation based on the atomic model in (h). (j–m) High-magnification ADF-STEM image series showing the step-by-step nanopore formation mechanism and the migration dynamics of a single Mo atom. Cyan and yellow dashed circles represent Mo and S atoms, respectively. The red dashed circle indicates the single Mo atom that relocated from the lattice to form the hole. Yellow arrows indicate the missing S atoms during the nanopore drilling process. (n) High-magnification ADF-STEM image showing the detailed configuration of a triangular sub-nanometre pore. (o) DFT-calculated atomic model corresponding to (n). (p) ADF-STEM image simulation based on the atomic model in (o). (q) Intensity line profiles measured along three zigzag directions, marked 1, 2 and 3, respectively, to show the interatomic distances between Mo atoms around the sub-nanometer pore. The region marked by the yellow background indicates the distance between two unsaturated Mo atoms at the pore edge along three zigzag directions. (r) Plots showing the interatomic distance variations for 5 different Mo-Mo gaps labelled by numbers in (q) along three zigzag orientations.

To further understand the formation mechanism of the sub-nanometer pore and its stability, we acquired dynamic data by imaging with a higher frame rate (see figure S2, S3). The formation of one triangular sub-nanometer pore needs the central Mo atom to escape from its original lattice location. As depicted in figure 4(i) (a)–(f), the central Mo atom (red dashed circle) spent more than 25s interacting with the surrounding six Mo atoms (blue dashed circles). The Mo atom breaks from the original lattice site and relocates to the surface when a neighbouring Mo atom undergoes a large displacement within the lattice, (figures 4(i) (g)) and then migrates (figures 4(i) (h)–(j)). The DFT calculation in figure 6 shows that when MoS<sub>2</sub> loses a single Mo atom and its surrounding three pair of S atoms, the ejected Mo atom has high probability to return to the middle of the pore (figures 6(a), (e) and (i)). Hence, the creation of a stable nanopore requires enough energy to be transferred to a Mo atom so that it can migrate away sufficiently from its original position. The ejected Mo atom migrates on the lattice surface, mainly around the nanopore edges, and resides at different positions (red dashed



circles in figure 4 (ii)). However, it seldom resides on the top of the Mo site, which is also supported by the lowest stability of such configurations from the DFT calculations in figure 6. The sub-coordinated Mo atoms on the nanopore edge are active and can move to different locations around the edge (pink dashed circles in figures 4(ii) (b–c) and green dashed circles in figures 4 (ii) (f–h)), leading to delocalization of the nanopore. In addition, S atoms at the nanopore edge also frequently migrate (yellow arrows in figure 4s (ii) (c–e)).

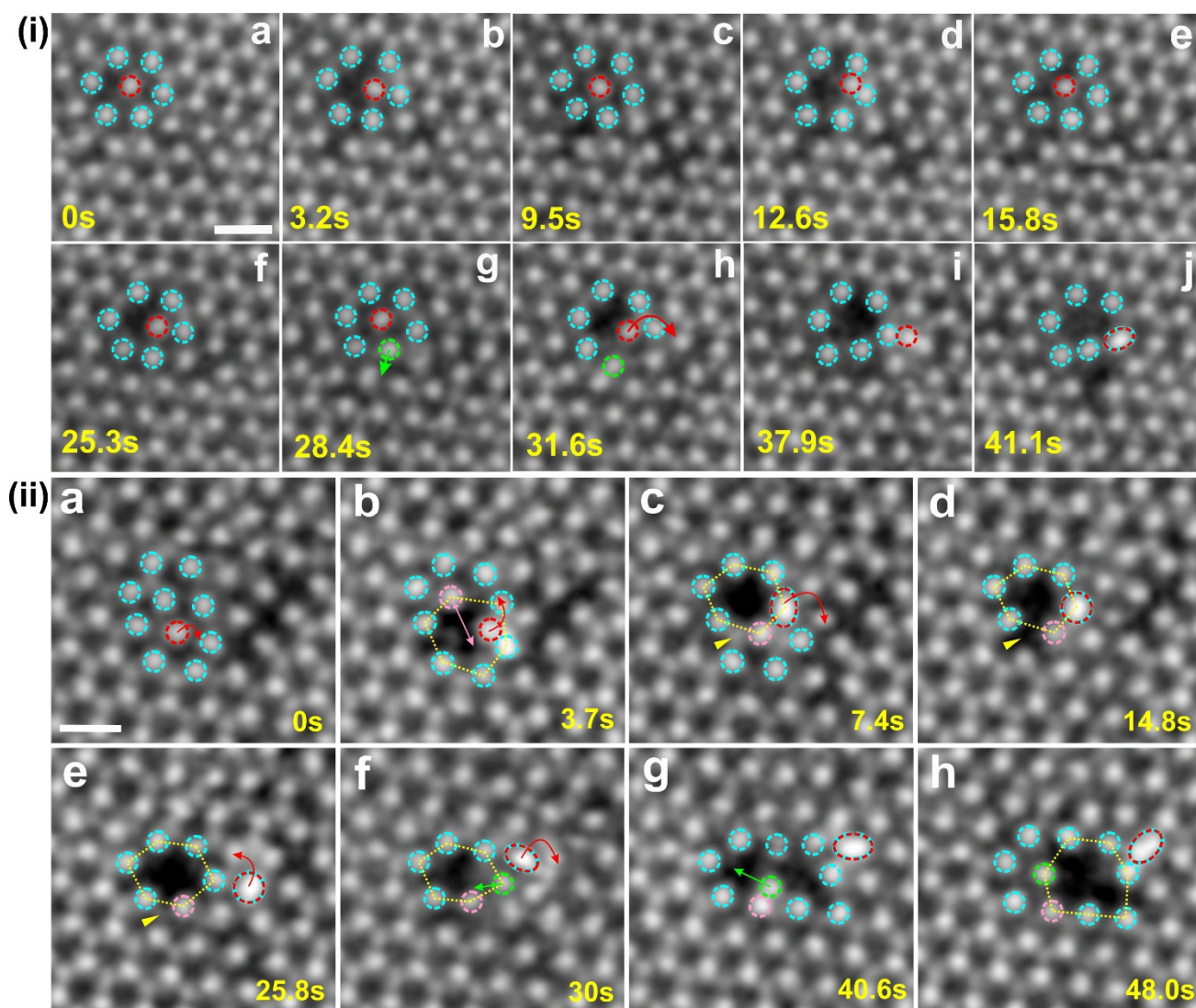


**Figure 4. Formation dynamics and stability of ultra-small nanopores. 80kV accelerating voltage** ((i) Time series of ADF-STEM images showing the detailed formation dynamics of a sub-nanometer pore formed from the loss of one Mo atom from its original lattice site and reattachment to the MoS<sub>2</sub> lattice surface close to the nanopore edge. Mo atoms on the nanopore edges are marked by the cyan dashed circles. Red dashed circles are

used to highlight the movements of the ejected Mo atom. The green circle in (g) and (h) shows the large displacement of one Mo atom at the nanopore edge which facilitates the escape of the central Mo atom from its original lattice site. (ii) Time series of ADF-STEM images showing the migration of the ejected Mo atom around the nanopore and the delocalization of the nanopore due to active movements of the edge atoms. The yellow dashed hexagonal boxes highlight the nanopore positions at different steps. The edge atoms that are displaced are marked by pink and green dashed circles. All scale bars correspond to 0.5 nm.

It was also possible to create the sub-nm pores using a 60kV accelerating voltage, instead of 80kV (figure S4, S5), as shown in figure 5f. To demonstrate that the sub-nm pores can be fabricated with a high degree of spatial precision we created multiple nanopores within the MoS<sub>2</sub>. We also varied the drilling time to create two different diameter holes ranging from the near ultimate small scale limit of ~0.6nm for a single missing Mo atom, figure 5, to the larger 1nm nanopores. Drill times were similar to those used for 80kV. A drilling time of ~10s was used to produce the 0.6nm holes, while a drilling time of ~30s led to larger 1nm nanopores, as previously demonstrated in figure 2. Figure 5a shows the pristine area of MoS<sub>2</sub> before drilling and figure 5b after drilling 3 nanopores in a vertical line using 30s drilling time for each. Figure 5c shows the area after drilling another nanopore for 30s, top right, followed by a smaller hole beneath it using only a 10s drill time. Figure 5e shows the area after drilling another two small holes formed using a 10s drilling time, where the holes formed with a 10s drilling time are indicated with red dashed circles and the holes formed with 30s drilling time with yellow dashed circles. The atomic structures of the two small holes drilled with 10s drilling time are shown in figure 5d and reveal that only one Mo atom is missing from the lattice, plus several surrounding S atoms (see figure S6). The individual Mo atom that was displaced from each nanopore is located on the surface nearby, evident as a single bright contrast spot.

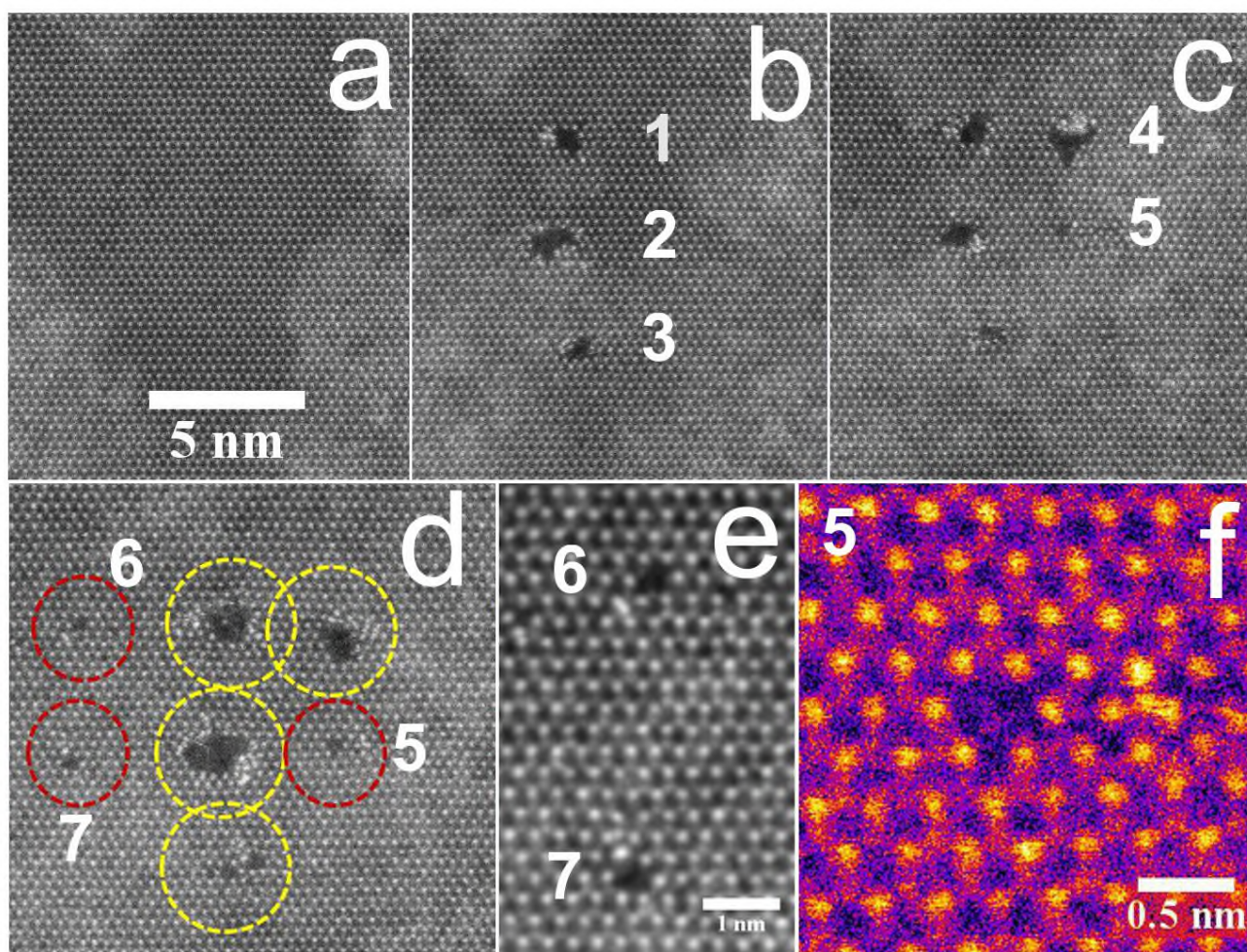


**Figure 5. Creating a 2D array of nanopores with different diameters using 60kV accelerating voltage.** (a) ADF-STEM image of the pristine area before drilling. (b) ADF-STEM image taken of the same area as in (a), but after drilling three nanopores (pores 1, 2 and 3) using a 30s exposure (slow scan). (c) ADF-STEM image taken of the same area as in panel b, but after drilling another hole using a 30s exposure (Pore 4) and a smaller one using a 10s exposure time (pore 5). (d) ADF-STEM image taken after drilling two further nanopores using a 10s exposure time (pores 6 and 7) (e) High magnification ADF-STEM image of pores 6 and 7 from figure 5d. (f) High magnification ADF-STEM image of pore 5, with false colour used to highlight the brighter contrast associated with the Mo atom displaced to the surface on the right of the pore.



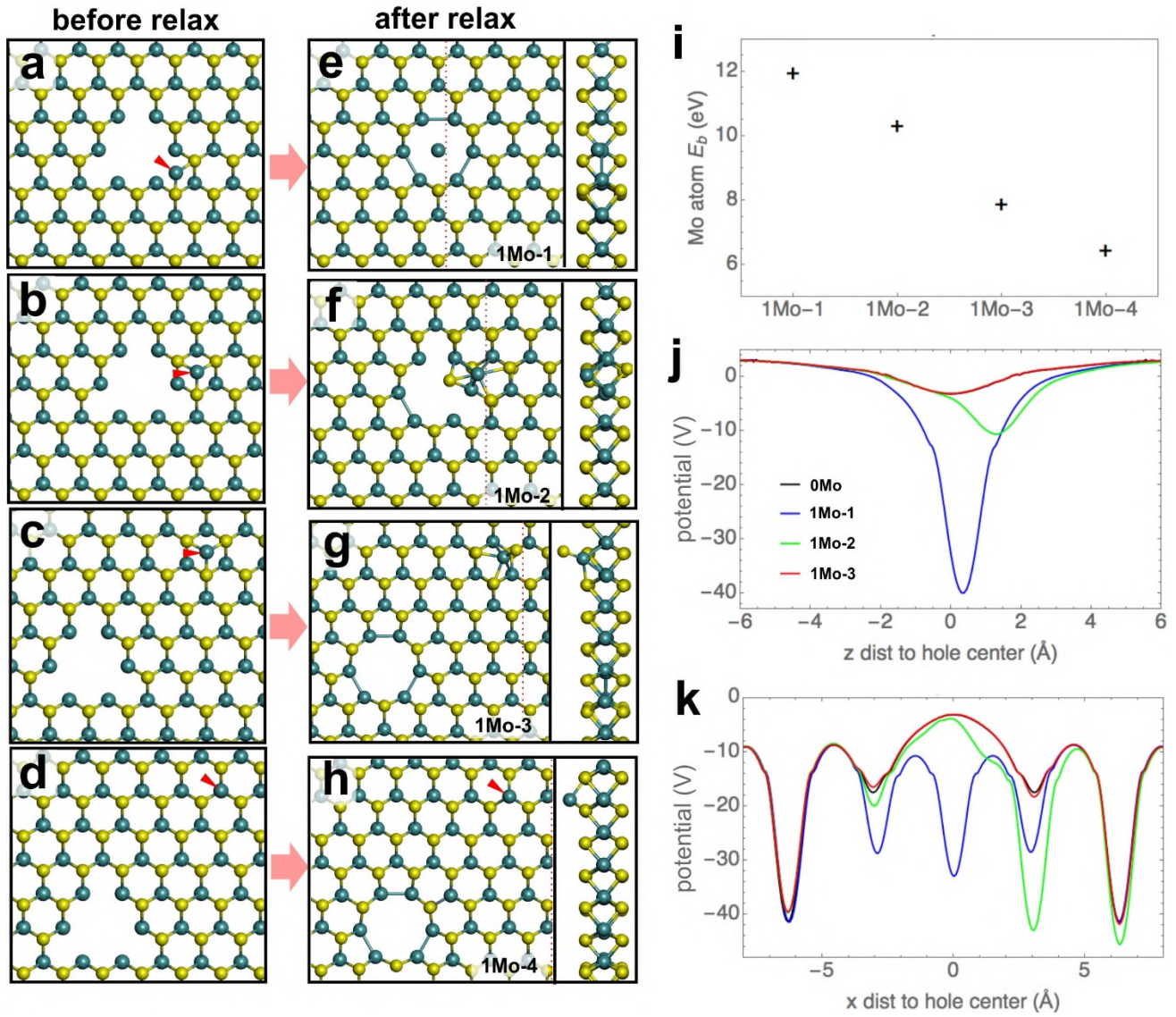


**Figure 6.** DFT calculations showing the energetically favourable structures of the sub-nanometer pore with the ejected single Mo atom attached to different locations on the MoS<sub>2</sub> monolayer surface. (a–d) Initial and (e–h) final structures following geometry optimization for the 4 different possible configurations of the sub-nanometer pore, with the red arrows indicating the positions of the ejected Mo atom. Side views from the cross sections marked by the red dashed lines are shown in the right panels. (i) Site dependent binding energies of the ejected Mo atom on the sheet surface. (j–k) Potential profile of the nanopores as a function of the distance between the ejected Mo atom and the hole centre along the z and x directions, respectively. 0 Mo denotes the nanopore assuming the ejected Mo atom has escaped from the surface, while the remaining legends are consistent with (a)–(h).

We have also conducted DFT calculations to investigate the stability of sub-nanometer pores by varying the attached locations of the ejected single Mo atom on the MoS<sub>2</sub> surface (with their formation energies provided in Table S1). Figures 6 (a)-(d) show the four initial states proposed formed by attaching the ejected Mo atoms to different locations on the MoS<sub>2</sub> surface, as marked by the red arrows, while figure 6 (e)-(h) show the corresponding relaxed structures based on DFT calculations. The binding energies ( $E_b$ ) of the ejected Mo atoms staying on the sheet surface in the above configurations are summarized in figure 6(i). Structures where the ejected Mo atoms stay on the MoS<sub>2</sub> sheets containing the nanopores is energetically favourable regardless of their position and configuration, consistent with experimental observations. For nanopores composed of a single Mo atom with its coordinated six S atoms, the ejected Mo atom can return to the middle of the nanopore without activation (figure 6(e)), which agrees well with the nanopore formation dynamics in figure 4 (i). In contrast, having the ejected Mo atom located on the top of the Mo site of the MoS<sub>2</sub> monolayer is relatively unstable. In addition, the location of the ejected Mo atoms is energetically favoured for sites located close to the nanopore on the MoS<sub>2</sub> surface when compared to more distant sites (figures 6 (f) and (g)) and to small clusters of Mo atoms (see figure S7, S8). Figures 6 (j) and (k) show potential profiles of a nanopore as a function of the z distance and x distance between the ejected Mo atom and the nanopore center, respectively. The z direction is defined as being perpendicular to the MoS<sub>2</sub> sheet, while the x direction is associated with one zigzag direction of the MoS<sub>2</sub> sheet. The nanopore potential profiles show great sensitivity to the local structure when the ejected Mo atom is close to the nanopore. However, this effect fades quickly with increasing distance between the ejected Mo atom and the nanopore as illustrated by the overlap of the black and red curves in figure 6 j-k, implying that screening is strong within the MoS<sub>2</sub> sheet. While our work focus on pristine nanopores, latest theoretical studies reveal the potential to achieve novel properties by advanced functionalization. For example, p-type MoS<sub>2</sub> may be realized in O passivated nanopores;<sup>54</sup> ferromagnetism may be induced by appropriate dopants;<sup>55</sup> spin splitting may be controlled by spin-orbit coupling in MXY (M= Mo, W

and X, Y =S, Se, Te).<sup>56</sup> These new phenomena open an opportunity to produce novel electronic, spintronic and valleytronic devices.

## Conclusion

In summary, we have shown that nucleation of a nanopore in monolayer MoS<sub>2</sub> at accelerating voltages of 60kV and 80kV is initiated by the local depletion of S by the electron beam, which destabilizes the Mo bonding and leads to a single Mo atom being ejection to the surface. The small 0.6nm nanopore only stabilizes when the Mo migrates away from the pore across the surface of MoS<sub>2</sub> and cannot hop back in, or when trapped in S vacancies. Because this process can be tracked in real time *in-situ* it is possible to control it to create sub-nm pores on demand with positional spacing of 1nm accuracy. The electron beam induced loss of S results in a Mo rich edge termination of the nanopores. The nanopore size can be tuned from an ultra-small triangular hole consisting of a vacancy produced by the removal of a single Mo atom and its coordinated six S atoms, to several nanometres by adjusting the scanning rate. Nanoscale patterning of nanopore arrays was fabricated by drilling holes one-by-one with demonstrated spacings to 4.2nm and with uniformity in the average nanopore diameter within the array.

## Methods

### *Synthesis and transfer of monolayer MoS<sub>2</sub>*

MoS<sub>2</sub> single layers were prepared using a similar approach to that previously reported.<sup>53</sup> Molybdenum trioxide (MoO<sub>3</sub>, ≥99.5%, Sigma-Aldrich) and sulphur (S, ≥99.5%, Sigma-Aldrich) powder were used to grow monolayer MoS<sub>2</sub> on a SiO<sub>2</sub>/Si substrate (300 nm thick SiO<sub>2</sub>) by chemical vapour deposition (CVD) at atmospheric pressure. Two furnaces were used to enable temperature control on both the precursors and the substrate. The heating temperatures for S, MoO<sub>3</sub> and SiO<sub>2</sub>/Si substrate were ~ 180, ~300, and ~800 °C, respectively, with argon used as the carrier gas. To avoid cross-contamination between MoO<sub>3</sub> and S, MoO<sub>3</sub> powder was placed in an inner tube having a smaller diameter, which

was then inserted into the larger 1-inch quartz tube. The S powder was loaded in the outer quartz tube. The substrate was oriented vertically to increase the uniform growth area of MoS<sub>2</sub> film. Monolayer MoS<sub>2</sub> was transferred onto the Si<sub>3</sub>N<sub>4</sub> TEM grid (Agar Scientific AG21580) *via* a standard polymer-based method.<sup>14</sup> The surface of the MoS<sub>2</sub>/SiO<sub>2</sub>/Si substrate was first spin-coated with a thin film of poly (methyl methacrylate) (PMMA) followed by floating it on a 1 M potassium hydroxide (KOH) solution to etch the SiO<sub>2</sub> away. After the PMMA/MoS<sub>2</sub> film was detached from the Si substrate, the film was rinsed in deionized water several times and then transferred to a holey Si<sub>3</sub>N<sub>4</sub> grid. It was dried overnight in air followed by baking at 180 °C for 15 minutes. Finally, the grid was submerged in acetone for 8 hours to remove PMMA.

#### *Scanning transmission electron microscopy*

Room temperature ADF-STEM imaging was performed on an aberration corrected JEOL ARM300CF STEM equipped with a JEOL ETA corrector<sup>57</sup> operated at an accelerating voltage of 80 kV (Figures 1 and 4), and 60 kV (Figures 5e-g) located in the electron Physical Sciences Imaging Centre (ePSIC) at Diamond Light Source. At 80 kV, the convergence semi-angle was 24.6 mrad with a camera length of 20cm, which gave an annular recording range of 39-156mrad at the detector. The electron probe diameter was focused to ~52pm. The beam current was measured as 23 pA using a Pico ampere meter for both the STEM imaging and sculpting mode. The spherical aberration (C<sub>s</sub>) and chromatic aberration (C<sub>c</sub>) were measured to be 1.2µm and 1.0mm, respectively. At 60 kV, the convergence semi-angle was 31.5 mrad with a camera length of 16cm, enabling the annular detector to record sufficient diffracted electron beams from the specimen in an angular range of 49.5–198mrad. The beam current was measured to be 44 pA. The spherical aberration (C<sub>s</sub>) and chromatic aberration (C<sub>c</sub>) were 0.4 µm and 0.89mm, respectively.

#### *Nanopore drilling*

Typical ‘fast-scanning’ ADF-STEM images were recorded with dwell times of 10-20 $\mu$ s per pixel across regions of  $\sim 20\text{nm} \times 20\text{nm}$ . A box was then used to define the area to be drilled based on the fast scan rate image previously acquired. The size of the box was adjustable and tailored to the total area exposed to the beam and the final size of the pore. We found that box sizes encompassing 4-6 Mo atoms ( $\sim 1\text{-}2\text{nm}$ ) were ideal for creating sub-nanometer holes in MoS<sub>2</sub> with excellent reproducibility. In order to drill a nanopore into the MoS<sub>2</sub>, the scan within the boxed area was set to a slower rate used for standard imaging to increase the beam current density received by each atom. This was adjusted to give the desired hole size within a specific time period and typically required a dwell time of  $\sim 30\mu\text{s}$  per pixel for a  $40 \times 40$  pixel region covering an area of  $\sim 1\text{nm} \times 1\text{nm}$ . Periods of exposure were adjusted from 10-30 seconds to control the average final pore size. In our experiments we were able to reliably create sub-nanometer pores in MoS<sub>2</sub> with a 10-30s total exposure time within the boxed region of  $\sim 1\text{nm} \times 1\text{nm}$ . After drilling, a ‘fast-scan’ ADF-STEM image was taken of the larger area to confirm that the pore was formed. These ultra-small nanopores can be easily engineered into the MoS<sub>2</sub> lattice at specific locations in a single step process by using the slow scan rate as in figure 2 and with a drilling time of 10s. However, the stochastic nature of atomic displacement by the electron beam means that this will not have 100% success and we found success rates of typically 80% in this work. However if no hole is produced in the first instance, then the process can be repeated. *In-situ* monitoring of the sample during the drilling process also helps to track the atomic displacements and judge the progression and success of the pore formation. In addition, large nanopores can also be easily drilled by applying a larger area and a longer dwell time (figure S9).

The image series in figure 4 were recorded using an exposure time of 1.31 s for each frame and with an interval between every two images of 1.85s for figure 4(i). For figure 4(ii), the exposure time and the interval are 1.84s and 1.85s, respectively.

#### *Image processing*

Images were processed using the ImageJ software. Some of them were adjusted with a Gaussian blur ( $\sim 2$  pixels) to smooth out the noise. Some grayscale images were inverted and false colour LUT was applied to improve the visualization. Atomic models were generated by the software of Accelrys Discovery Studio Visualizer. Multislice ADF image simulation based on the corresponding atomic model were carried out using the JEMS software package with parameter settings matching individual experimental conditions: 4 nm defocus, 5.3 nm defocus spread, 80 kV accelerating voltage,  $C_c = 1.0$  mm, energy spread of 0.80 eV,  $C_s = 1.2$   $\mu$ m, 24.6 mrad half convergence angle. Weickenmeier-Kohn atomic form factors were used with core and phonon absorption with 600 K frozen phonons.

#### *Density Functional Theory (DFT) calculation*

Standard *ab-initio* calculations within the framework of density-functional theory (DFT) were carried out to optimize the geometry and explore the potential profile of nanopores with various configurations, using the Vienna *Ab Initio* Simulation Package (VASP v5.4).<sup>58</sup> Plane-wave and projector-augmented-wave (PAW) type pseudopotentials with kinetic-energy cutoffs of up to 400 eV were applied, with the GGA-PBE exchange-correlation functional.<sup>59,60</sup> Van der Waals interaction was accounted by DFT-D2 method of Grimme,<sup>61</sup> with the cutoff radius for pair interactions set to 50 Å. The 8×4 rectangular supercells containing 192 atoms along with a 20 Å vacuum perpendicular to the sheet were constructed to avoid artificial interactions between periodic images. Dipole correction<sup>62</sup> was employed to address the leading errors in both energy and potential caused by periodic boundary condition imposed on highly asymmetric surfaces. We verified that the impact of spin-polarization is non-negligible but much smaller than the configuration-dependent fluctuations (Supporting information section S9), and therefore was not taken into account in the remaining calculations. The structures were relaxed until all forces were smaller than 0.02 eV/Å. The  $\Gamma$  point was used for relaxation, while a Monkhorst-Pack k-point grids of 3×3×1 was adopted in obtaining binding energies and potential profiles.<sup>63</sup> Given our



purpose of qualitatively illustrating the stability of nanopores and the strong dependence of potential profile on nanopore configuration, the spin-orbit coupling effect was neglected in this study.

**Conflict of Interest:** The authors declare no competing financial interest.

## Acknowledgements

JHW thanks the Royal Society for support. SW thanks the China Scholarship Council for support. AIK acknowledges EPSRC support under platform grant EP/K032518/1.

## References

- 1 A. K. Geim and K. S. Novoselov, *Nat. Mater.*, 2007, **6**, 183–191.
- 2 S. Z. Butler, S. M. Hollen, L. Cao, Y. Cui, J. A. Gupta, H. R. Gutierrez, T. F. Heinz, S. S. Hong, J. Huang, A. F. Ismach, E. Johnston-Halperin, M. Kuno, V. V. Plashnitsa, R. D. Robinson, R. S. Ruoff, S. Salahuddin, J. Shan, L. Shi, M. G. Spencer, M. Terrones, W. Windl and J. E. Goldberger, *ACS Nano*, 2013, **7**, 2898–2926.
- 3 L. Song, L. Ci, H. Lu, P. B. Sorokin, C. Jin, J. Ni, A. G. Kvashnin, D. G. Kvashnin, J. Lou, B. I. Yakobson and P. M. Ajayan, *Nano Lett.*, 2010, **10**, 3209–3215.
- 4 Q. H. Wang, K. Kalantar-Zadeh, A. Kis, J. N. Coleman and M. S. Strano, *Nat. Nanotechnol.*, 2012, **7**, 699–712.
- 5 D. Jariwala, V. K. Sangwan, L. J. Lauhon, T. J. Marks and M. C. Hersam, *ACS Nano*, 2014, **8**, 1102–1120.
- 6 A. Splendiani, L. Sun, Y. Zhang, T. Li, J. Kim, C.-Y. Chim, G. Galli and F. Wang, *Nano Lett.*, 2010, **10**, 1271–1275.
- 7 B. Radisavljevic, A. Radenovic, J. Brivio, V. Giacometti and A. Kis, *Nat. Nanotechnol.*, 2011, **6**, 147–150.

- 8 Y. Li, Z. Zhou, S. Zhang and Z. Chen, *J. Am. Chem. Soc.*, 2008, **130**, 16739–16744.
- 9 I. S. Kim, V. K. Sangwan, D. Jariwala, J. D. Wood, S. Park, K.-S. Chen, F. Shi, F. Ruiz-Zepeda, A. Ponce, M. Jose-Yacaman, V. P. Dravid, T. J. Marks, M. C. Hersam and L. J. Lauhon, *ACS Nano*, 2014, **8**, 10551–10558.
- 10 H. J. Conley, B. Wang, J. I. Ziegler, R. F. Haglund, S. T. Pantelides and K. I. Bolotin, *Nano Lett.*, 2013, **13**, 3626–3630.
- 11 S. K C, R. C. Longo, R. Addou, R. M. Wallace and K. Cho, *Nanotechnology*, 2014, **25**, 375703.
- 12 Y. C. Lin, D. O. Dumcenco, H.-P. Komsa, Y. Niimi, A. V. Krashenninnikov, Y.-S. Huang and K. Suenaga, *Adv. Mater.*, 2014, **26**, 2857–2861.
- 13 K. Zhang, S. Feng, J. Wang, A. Azcatl, N. Lu, R. Addou, N. Wang, C. Zhou, J. Lerach, V. Bojan, M. J. Kim, L.-Q. Chen, R. M. Wallace, M. Terrones, J. Zhu and J. A. Robinson, *Nano Lett.*, 2015, **15**, 6586–6591.
- 14 S. Wang, G.-D. Lee, S. Lee, E. Yoon and J. H. Warner, *ACS Nano*, 2016, **10**, 5419–5430.
- 15 Y.-C. Lin, D. O. Dumcenco, Y.-S. Huang and K. Suenaga, *Nat. Nanotechnol.*, 2014, **9**, 391–396.
- 16 W. Zhou, X. Zou, S. Najmaei, Z. Liu, Y. Shi, J. Kong, J. Lou, P. M. Ajayan, B. I. Yakobson and J.-C. Idrobo, *Nano Lett.*, 2013, **13**, 2615–2622.
- 17 Y. Gong, Z. Liu, A. R. Lupini, G. Shi, J. Lin, S. Najmaei, Z. Lin, A. L. Elías, A. Berkdemir, G. You, H. Terrones, M. Terrones, R. Vajtai, S. T. Pantelides, S. J. Pennycook, J. Lou, W. Zhou and P. M. Ajayan, *Nano Lett.*, 2014, **14**, 442–449.
- 18 O. Lehtinen, H. Komsa, A. Pulkin, M. B. Whitwick, M. Chen, T. Lehnert, M. J. Mohn, O. V

- Yazyev, A. Kis, U. Kaiser and A. V Krashennnikov, *ACS Nano*, 2015, **9**, 3274–3283.
- 19 H. Liu, L. Jiao, F. Yang, Y. Cai, X. Wu, W. Ho, C. Gao, J. Jia, N. Wang, H. Fan, W. Yao and M. Xie, *Phys. Rev. Lett.*, 2014, **113**, 066105.
  - 20 D. Cohen-Tanugi and J. C. Grossman, *Nano Lett.*, 2012, **12**, 3602–3608.
  - 21 S. P. Surwade, S. N. Smirnov, I. V. Vlassiouk, R. R. Unocic, G. M. Veith, S. Dai and S. M. Mahurin, *Nat. Nanotechnol.*, 2015, **10**, 459–464.
  - 22 M. Heiranian, A. B. Farimani and N. R. Aluru, *Nat. Commun.*, 2015, **6**, 8616.
  - 23 S. Kuran, S. Samitsu, X. Peng, K. Kurashima and I. Ichinose, *Science*, 2012, **335**, 444–447.
  - 24 H. W. Kim, H. W. Yoon, S.-M. Yoon, B. M. Yoo, B. K. Ahn, Y. H. Cho, H. J. Shin, H. Yang, U. Paik, S. Kwon, J.-Y. Choi and H. B. Park, *Science*, 2013, **342**, 91–95.
  - 25 H. W. C. Postma, *Nano Lett.*, 2010, **10**, 420–425.
  - 26 S. K. Min, W. Y. Kim, Y. Cho and K. S. Kim, *Nat. Nanotechnol.*, 2011, **6**, 162–165.
  - 27 G. F. Schneider, S. W. Kowalczyk, V. E. Calado, G. Pandraud, H. W. Zandbergen, L. M. K. Vandersypen and C. Dekker, *Nano Lett.*, 2010, **10**, 3163–3167.
  - 28 J. Feng, K. Liu, M. Graf, D. Dumcenco, A. Kis, M. Di Ventura and A. Radenovic, *Nat. Mater.*, 2016, **15**, 850–855.
  - 29 J. Feng, K. Liu, M. Graf, M. Lihter, R. D. Bulushev, D. Dumcenco, D. T. L. Alexander, D. Krasnozhan, T. Vuletic, A. Kis and A. Radenovic, *Nano Lett.*, 2015, **15**, 3431–3438.
  - 30 S. Garaj, S. Liu, J. A. Golovchenko and D. Branton, *Proc. Natl. Acad. Sci. U. S. A.*, 2013, **110**, 12192–12196.
  - 31 K. Liu, J. Feng, A. Kis and A. Radenovic, *ACS Nano*, 2014, **8**, 2504–2511.

- 32 M. L. Gethers, J. C. Thomas, S. Jiang, N. O. Weiss, X. Duan, W. A. Goddard and P. S. Weiss, 2015, **9**, 10909–10915.
- 33 X. G. Han, M. R. Funk, F. Shen, Y.-C. Chen, Y. Li, C. J. Campbell, J. Q. Dai, X. F. Yang, J.-W. Kim, Y. Liao, J. W. Connell, V. Barone, Z. Chen, Y. Lin and L. Hu, *ACS Nano*, 2014, **8**, 8255–8265.
- 34 J. Bai, X. Zhong, S. Jiang, Y. Huang and X. Duan, *Nat. Nanotechnol.*, 2010, **5**, 190–194.
- 35 Y. Huang, J. Wu, X. Xu, Y. Ho, G. Ni, Q. Zou, G. K. W. Koon, W. Zhao, A. H. Castro Neto, G. Eda, C. Shen and B. Özyilmaz, *Nano Res.*, 2013, **6**, 200–207.
- 36 A. W. Robertson, G.-D. Lee, K. He, C. Gong, Q. Chen, E. Yoon, A. I. Kirkland and J. H. Warner, *ACS Nano*, 2015, **9**, 11599–11607.
- 37 B. Song, G. F. Schneider, Q. Xu, G. Pandraud, C. Dekker and H. Zandbergen, *Nano Lett.*, 2011, **11**, 2247–2250.
- 38 Q. Xu, M.-Y. Wu, G. F. Schneider, L. Houben, S. K. Malladi, C. Dekker, E. Yucelen, R. E. Dunin-Borkowski and H. W. Zandbergen, *ACS Nano*, 2013, **7**, 1566–1572.
- 39 M. D. Fischbein and M. Drndić, *Nano Lett.*, 2007, **7**, 1329–1337.
- 40 J. A. Rodriguez-Manzo, A. V. Krasheninnikov and F. Banhart, *ChemPhysChem*, 2012, **13**, 2596–2600.
- 41 F. Börrnert, L. Fu, S. Gorantla, M. Knupfer, B. Büchner and M. H. Rummeli, *ACS Nano*, 2012, **6**, 10327–10334.
- 42 J. A. Rodriguez-Manzo and F. Banhart, *Nano Lett.*, 2009, **9**, 2285–2289.
- 43 M. D. Fischbein and M. Drndić, *Appl. Phys. Lett.*, 2008, **93**, 2006–2009.
- 44 P. Masih Das, G. Danda, A. Cupo, W. M. Parkin, L. Liang, N. Kharche, X. Ling, S. Huang,

- M. S. Dresselhaus, V. Meunier and M. Drndic, *ACS Nano*, 2016, **10**, 5687–5695.
- 45 D. Emmrich, A. Beyer, A. Nadzeyka, S. Bauerdick, J. C. Meyer, J. Kotakoski and A. Götzhäuser, *Appl. Phys. Lett.*, 2016, **108**, 163103.
- 46 J. C. Meyer, A. Chuvilin, G. Algara-Siller, J. Biskupek and U. Kaiser, *Nano Lett.*, 2009, **9**, 2683–2689.
- 47 T. Xu, X. Xie, K. Yin, J. Sun, L. He and L. Sun, *Small*, 2014, **10**, 1724–1728.
- 48 J. Lin, O. Cretu, W. Zhou, K. Suenaga, D. Prasai, K. I. Bolotin, N. T. Cuong, M. Otani, S. Okada, A. R. Lupini, J.-C. Idrobo, D. Caudel, A. Burger, N. J. Ghimire, J. Yan, D. G. Mandrus, S. J. Pennycook and S. T. Pantelides, *Nat. Nanotechnol.*, 2014, **9**, 436–442.
- 49 H.-P. Komsa, J. Kotakoski, S. Kurasch, O. Lehtinen, U. Kaiser and A. V. Krasheninnikov, *Phys. Rev. Lett.*, 2012, **109**, 035503.
- 50 J. Lin, S. T. Pantelides and W. Zhou, *ACS Nano*, 2015, **9**, 5189–5197.
- 51 R. Zan, Q. M. Ramasse, R. Jalil, T. Georgiou, U. Bangert and K. S. Novoselov, *ACS Nano*, 2013, **7**, 10167–10174.
- 52 H.-P. Komsa, S. Kurasch, O. Lehtinen, U. Kaiser and A. V. Krasheninnikov, *Phys. Rev. B*, 2013, **88**, 035301.
- 53 S. Wang, M. Pacios, H. Bhaskaran and J. H. Warner, *Nanotechnology*, 2016, **27**, 85604–85611.
- 54 L. Y. Gan, Y. Cheng, U. Schwingenschlögl, Y. Yao, Y. Zhao, X. X. Zhang and W. Huang, *Appl. Phys. Lett.*, 2016, **109**, 091603.
- 55 Y. C. Cheng, Z. Y. Zhu, W. B. Mi, Z. B. Guo and U. Schwingenschlögl, *Phys. Rev. B*, 2013, **87**, 100401.

- 56 Y. C. Cheng, Z. Y. Zhu, M. Tahir and U. Schwingenschlögl, *Europhys. Lett.*, 2013, **102**, 57001.
- 57 F. Hosokawa, H. Sawada, Y. Kondo, K. Takayanagi and K. Suenaga, *Microscopy*, 2013, **62**, 23–41.
- 58 G. Kresse and J. Furthmüller, *Phys. Rev. B*, 1996, **54**, 11169–11186.
- 59 P. E. Blochl, *Phys. Rev. B*, 1994, **50**, 17953–17979.
- 60 J. P. Perdew, K. Burke and M. Ernzerhof, *Phys. Rev. Lett.*, 1996, **77**, 3865–3868.
- 61 S. Grimme, *J. Comput. Chem.*, 2006, **27**, 1787–1799.
- 62 G. Makov and M. Payne, *Phys. Rev. B*, 1995, **51**, 4014–4022.
- 63 H. J. Monkhorst and J. D. Pack, *Phys. Rev. B*, 1976, **13**, 5188–5192.

### TOC graphic

